Journal of ELECTRONIC MATERIALS, Vol. 48, No. 10, 2019
https://doi.org/10.1007/s11664-019-07479-x

Synergistic Effects of Optical and Photoluminescence Properties, Charge Transfer, and Photocatalytic Activity in $MgAl_2O_4$:Ce and Mn-Codoped $MgAl_2O_4$:Ce Phosphors

SHIFA WANG,[1,2,6] CHAOLI CHEN,[1] YANWU LI,[1] QING ZHANG,[3] YANLAN LI,[3] and HUAJING GAO[4,5,7]

1.—School of Electronic and Information Engineering, Chongqing Three Gorges University, Chongqing, Wanzhou 404000, China. 2.—Chongqing Key Laboratory of Geological Environment Monitoring and Disaster Early-Warning in Three Gorges Reservoir Area, Chongqing Three Gorges University, Chongqing, Wanzhou 404000, China. 3.—School of Environmental and Chemical Engineering, Chongqing Three Gorges University, Chongqing, Wanzhou 404000, China. 4.—State Key Laboratory of Advanced Processing and Recycling of Non-ferrous Metals, Lanzhou University of Technology, Lanzhou 730050, China. 5.—School of Science, Lanzhou University of Technology, Lanzhou 730050, China. 6.—e-mail: wangshifa2006@yeah.net. 7.—e-mail: ghj2011@yeah.net

A gamma-ray irradiation-assisted polyacrylamide gel method has been used to synthesize $MgAl_2O_4$:Ce and Mn-codoped $MgAl_2O_4$:Ce phosphors. Ce ion doping improved the photoluminescence properties of $MgAl_2O_4$ but did not change the cubic spinel structure of the host. Transmission electron microscopy showed that the mean particle size of the Ce- and Mn-codoped $MgAl_2O_4$ nanoparticles was smaller than that of the $MgAl_2O_4$ nanoparticles. Ce and Mn codoping improved the light absorption capacity and utilization, the separation efficiency of photogenerated carriers, and the photocatalytic activity of the $MgAl_2O_4$ nanoparticles. The $MgAl_2O_4$:Ce:Mn nanoparticles exhibited high photocatalytic activity for photodegradation of methylene blue dye under simulated sunlight irradiation due to the synergistic effects of the band-edge position, the light absorption capacity and utilization, and the separation efficiency of photogenerated carriers.

Key words: Mn-codoped $MgAl_2O_4$:Ce phosphor, photoluminescence properties, light absorption capacity, photocatalytic activity, band-edge position

INTRODUCTION

Magnesium aluminate ($MgAl_2O_4$) has attracted particular interest for lightweight armor, electronic ceramics, infrared-transparent windows for use in strong radiation environments, luminescent matrix materials, microwave dielectric and ceramic capacitors, and photocatalysts due to its high thermal and chemical stability, low density, strong radiation resistance, nontoxicity, and high photocatalytic activity.[1–8] However, single $MgAl_2O_4$ phase exhibits only weak photoluminescence properties and must be irradiated by intense laser light (325 nm) to produce fluorescence.[9] Recently, various methods have been used to enhance the photoluminescence properties of single $MgAl_2O_4$ phase. One such method is to dope $MgAl_2O_4$ with rare-earth ions to produce luminescence centers in the host material.[10–14] More specifically, cerium (Ce) is of great significance as an activator, as the Ce ion can act as a photoluminescence emission center in host materials.[15–20] In addition, Mn, Bi, and other non-rare-earth ions can also be used as activators to improve the photoluminescence properties of host materials.[21–28] Mn ion doping enhances the photoluminescence properties of $MgAl_2O_4$ due to the $^4T_1$ to $^6A_1$

(Received May 9, 2019; accepted July 23, 2019; published online August 2, 2019)

transition of the Mn ion.[29–31] To the best of the authors' knowledge, the photoluminescence properties and photocatalytic activity of Mn-codoped $MgAl_2O_4$:Ce phosphor have not been studied yet.

The relationship between the photoluminescence properties and photocatalytic activity of semiconducting materials has not been determined. Dillon et al.[32] stated that the photoluminescence dynamics can be applied to evaluate the photocatalytic activity of semiconducting materials. Wei et al.[33] synthesized BiOBr by a one-pot solvothermal method, showing that the emission intensity increases with increasing photocatalytic activity due to variation of the oxygen vacancy concentration. Zhang et al.[34] found that the emission intensity decreases with increasing photocatalytic activity due to variation of the geometrical morphology. Xiao et al.[35] and Jing et al.[36] found that Sm^{3+}-doped TiO_2 and La-doped TiO_2 in nanocrystalline form showed stronger emission intensity and exhibited higher photocatalytic activity due to their different surface oxygen vacancies and defects. Sellappan et al.[37] synthesized TiO_2/carbon nanofilms that exhibited lower photoluminescence intensity, shorter carrier lifetime, and higher photocatalytic activity due to charge carrier transfer at the interfaces. Similar phenomena were observed by Cai et al.[38] Based on previous reports, the photoluminescence and photocatalytic activity of semiconducting materials probably originate from the band-edge position, light absorption capacity and utilization, and separation efficiency of photogenerated carriers. Therefore, it is of great significance to study the synergistic effects of the band-edge position, light absorption capacity and utilization, and separation efficiency of photogenerated carriers on photoluminescent properties and photocatalytic activity of $MgAl_2O_4$:Ce and Mn-codoped $MgAl_2O_4$:Ce phosphors.

The polyacrylamide gel method is a highly effective method for synthesis of semiconductor composite materials.[39–42] Recently, we developed a gamma-ray irradiation-assisted polyacrylamide gel route to synthesize metal oxide nanoparticles.[43,44] Metal oxide nanoparticles synthesized using this novel method exhibit special defect structure, resulting in enhanced physical and chemical properties. However, $MgAl_2O_4$:Ce and Mn-codoped $MgAl_2O_4$:Ce phosphors have yet to be synthesized using the gamma-ray irradiation-assisted polyacrylamide gel route.

The purpose of the work presented herein is threefold: (1) to synthesize $MgAl_2O_4$:Ce and Mn-codoped $MgAl_2O_4$:Ce phosphors using the gamma-ray irradiation-assisted polyacrylamide gel method, (2) to study the optical, photoluminescence, and photocatalytic properties of these phosphors, and (3) to study the synergistic effects of the band-edge position, the light absorption capacity and utilization, and the separation efficiency of photogenerated carriers on their photoluminescent properties and photocatalytic activity.

EXPERIMENTAL PROCEDURES

Synthesis of $MgAl_2O_4$:Ce and $MgAl_2O_4$:Ce:Mn Nanoparticles

Stoichiometric amounts of $Mg(NO_3)_2{\cdot}6H_2O$, $CeCl_3{\cdot}6H_2O$, $AlCl_3{\cdot}9H_2O$, and $Mn(CH_3COO)_2{\cdot}4H_2O$ were dissolved in deionized water to obtain a final solution of 0.015 mol/L of total cations. To obtain $MgAl_2O_4$:Ce and $MgAl_2O_4$:Ce:Mn nanoparticles, two solutions with different molar ratios of metal ions, viz. $n_{Mg,Al}{:}n_{Ce}$ = 9:1 and $n_{Mg,Al}{:}n_{Ce,Mn}$ = 9:1 ($n_{Ce}{:}n_{Mn}$ = 9:1), were configured. After the solution became transparent, 4.7282 g citric acid, 20 g glucose, 9.5958 g acrylamide, and 1.9192 g *N*,*N*′-methylene-bisacrylamide monomer were added to the solution. The resultant solution was exposed to a ^{60}Co γ-source to a dose of 20 kGy to initiate the polymerization reaction and obtain a jelly-like gel. The gel was dried at 120°C for 24 h, and some xerogel powder was calcined at 900°C for 5 h in air to prepare $MgAl_2O_4$:Ce and $MgAl_2O_4$:Ce:Mn nanoparticles.

Sample Characterization

The phase structure of the $MgAl_2O_4$:Ce and $MgAl_2O_4$:Ce:Mn nanoparticles was characterized by x-ray diffraction (XRD) analysis. The surface morphology of the $MgAl_2O_4$:Ce and $MgAl_2O_4$:Ce:Mn nanoparticles was analyzed by transmission electron microscopy (TEM). Ultraviolet–visible (UV–Vis) diffuse reflectance spectra of the $MgAl_2O_4$:Ce and $MgAl_2O_4$:Ce:Mn nanoparticles were collected on a UV-1800 UV–Vis spectrophotometer. The photoluminescence properties of the $MgAl_2O_4$:Ce and $MgAl_2O_4$:Ce:Mn nanoparticles were measured at room temperature by using a 970CRT fluorescence spectrophotometer. The electrochemical properties of the $MgAl_2O_4$:Ce and $MgAl_2O_4$:Ce:Mn nanoparticles were investigated by using a CST 350 electrochemical workstation with a three-electrode cell configuration as described in literature.[9] Photocatalytic degradation experiments using the $MgAl_2O_4$:Ce and $MgAl_2O_4$:Ce:Mn nanoparticles were carried out for degradation of methylene blue dye under irradiation by a 150-W/m^2 xenon lamp. The relevant photocatalytic experiment process is consistent with literature,[9] with only the photocatalyst being changed.

RESULTS AND DISCUSSION

Structure Analysis

Figure 1a shows the XRD patterns of the $MgAl_2O_4$:Ce and $MgAl_2O_4$:Ce:Mn samples. Based on literature,[9] the cubic $MgAl_2O_4$ phase is completely formed at 900°C. To obtain $MgAl_2O_4$:Ce and $MgAl_2O_4$:Ce:Mn without organics, $MgAl_2O_4$:Ce and $MgAl_2O_4$:Ce:Mn xerogels were sintered at 900°C. The XRD peaks observed for the two samples at 2θ

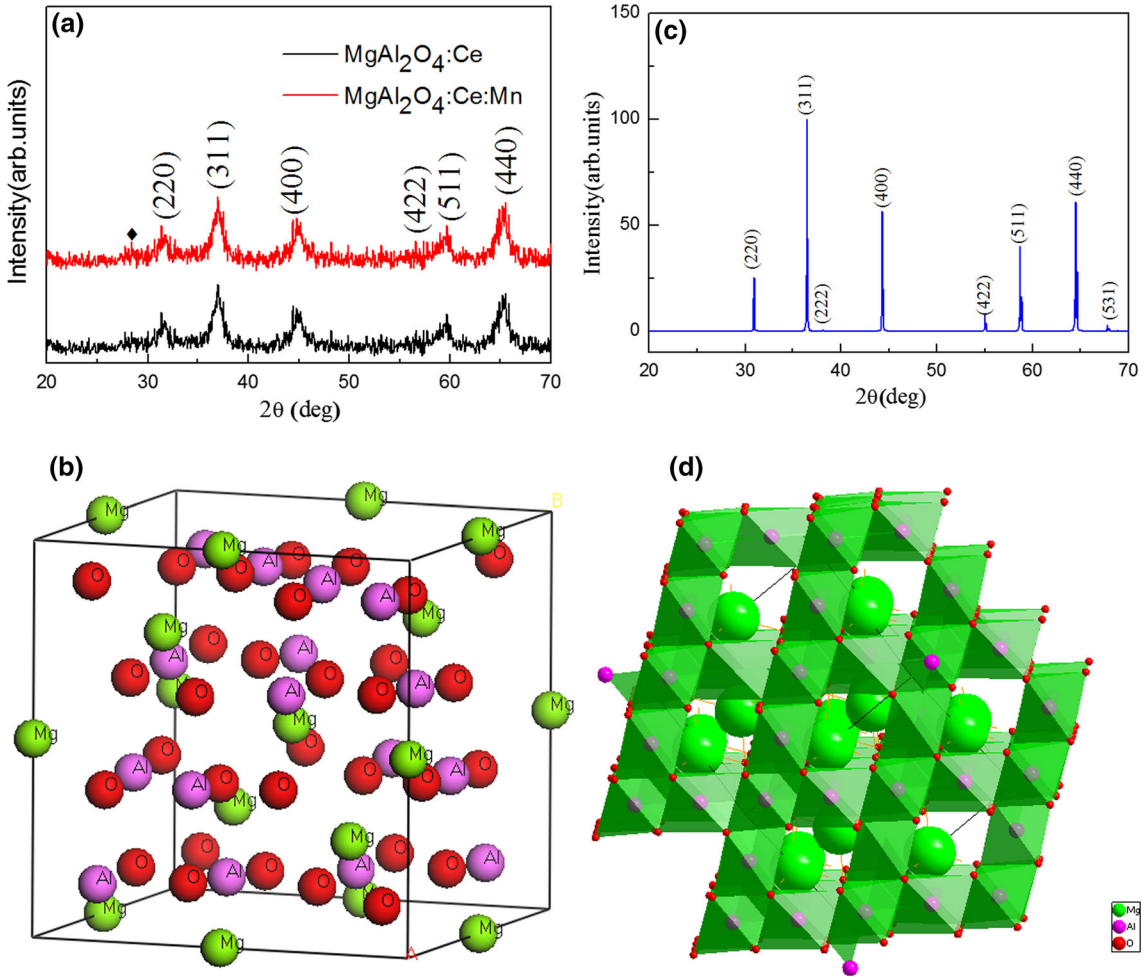

Fig. 1. (a) XRD patterns of $MgAl_2O_4$:Ce and $MgAl_2O_4$:Ce:Mn samples. (b) Unit cell structure of $MgAl_2O_4$. (c) XRD results for $MgAl_2O_4$. (d) Detailed crystal structure of $MgAl_2O_4$ in space group *Fd-3m*.

angles of 31.257°, 36.839°, 44.875°, 55.643°, 59.340°, and 65.239° can be assigned, respectively, to (220), (311), (400), (422), (511), and (440) planes of cubic $MgAl_2O_4$ phase, except for one peak marked by a black box (◆) which is ascribed to CeO_2. In Fig. 1a, the diffraction peaks of Mn oxide are unobserved. To obtain more accurate element compositional information for the $MgAl_2O_4$:Ce and $MgAl_2O_4$:Ce:Mn samples, energy-dispersive spectrometry (EDS) and high-resolution transmission electron microscopy (HRTEM) were applied. Figure 1b shows the unit cell structure of $MgAl_2O_4$. The XRD results of $MgAl_2O_4$ can be analyzed using the unit cell structure of $MgAl_2O_4$. In Fig. 1c, the diffraction peaks are similar to those in Fig. 1a except for two weak peaks at 2θ angles of 38.554° and 68.667°, which may be due to the introduction of Ce and Mn ions into the $MgAl_2O_4$ precursor to suppress formation of cubic $MgAl_2O_4$ phase.[9] The detailed crystal structure of cubic $MgAl_2O_4$ phase in space group *Fd-3m* is shown in Fig. 1d. It can be seen that magnesium (Mg), aluminum (Al), and oxygen (O) occupy Wyckoff positions 8a, 16d, and 32e, respectively.[13,45–47]

Figure 2a and b show TEM images of the $MgAl_2O_4$:Ce and $MgAl_2O_4$:Ce:Mn samples, respectively. The $MgAl_2O_4$:Ce and $MgAl_2O_4$:Ce:Mn nanoparticles were approximately spherical but seriously agglomerated. The mean particle size of the $MgAl_2O_4$:Ce and $MgAl_2O_4$:Ce:Mn samples was found to be 30 nm and 20 nm, respectively, as shown in Fig. 2c and d. Compared with the spinel $MgAl_2O_4$ nanoparticles, the mean particle size of the $MgAl_2O_4$:Ce:Mn nanoparticles was significantly smaller due to the introduction of the Ce and Mn metal salts into the $MgAl_2O_4$ precursor to suppress formation of $MgAl_2O_4$ phase.[9] Figure 2e shows a HRTEM image of the $MgAl_2O_4$:Ce sample, displaying lattice fringes with *d*-spacing of 0.1496 nm, 0.2025 nm, 0.2441 nm, and 0.2859 nm, which correspond to (440), (400), (311), and (220) planes of $MgAl_2O_4$, and lattice fringes with *d*-spacing of 0.1689 nm, which correspond to (311) plane of CeO_2. An HRTEM image of the $MgAl_2O_4$:Ce:Mn sample is shown in Fig. 2f, displaying a lattice spacing of 0.2038 nm between and among adjacent lattice planes that corresponds to (400) planes,

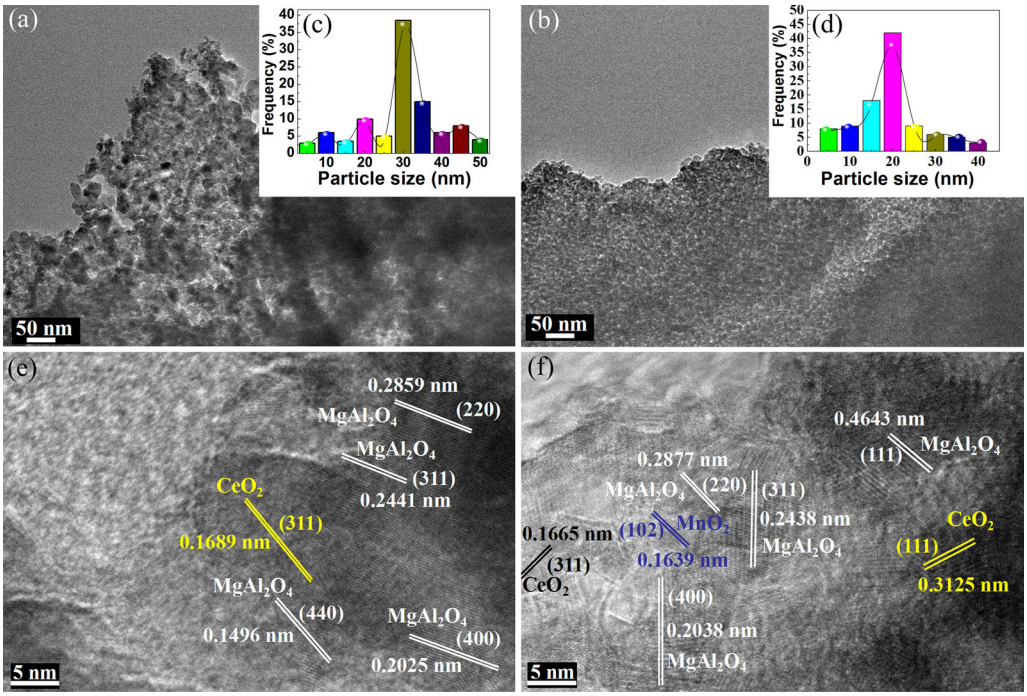

Fig. 2. TEM images of (a) $MgAl_2O_4$:Ce and (b) $MgAl_2O_4$:Ce:Mn samples. Particle size distribution of (c) $MgAl_2O_4$:Ce and (d) $MgAl_2O_4$:Ce:Mn samples. HRTEM images of (e) $MgAl_2O_4$:Ce and (f) $MgAl_2O_4$:Ce:Mn samples.

0.2438 nm that corresponds to (311) planes, 0.2877 nm that corresponds to (220) planes, and 0.4643 nm that corresponds to (111) planes of $MgAl_2O_4$. In addition, the lattice fringes with *d*-spacing of 0.1665 nm and 0.3125 nm correspond to (311) and (111) planes of CeO_2. The lattice fringes with *d*-spacing of 0.1639 nm correspond to (102) planes of MnO_2. These results indicate successful synthesis of $MgAl_2O_4$:Ce and $MgAl_2O_4$:Ce:Mn nanocomposites by the gamma-ray irradiation-assisted polyacrylamide gel method.

The elemental composition of the $MgAl_2O_4$:Ce and $MgAl_2O_4$:Ce:Mn samples was further studied by energy-dispersive spectrometry (EDS), as shown in Fig. 3. For the $MgAl_2O_4$:Ce sample (Fig. 3a), the major elements were found to be C, O, Ce, Mg, Al, and Cu,, while the major elements were C, O, Ce, Mg, Al, Mn, and Cu for the $MgAl_2O_4$:Ce:Mn sample, as shown in Fig. 3b. In Fig. 3, the characteristic peaks of C and Cu elements are ascribed to the carbon copper micromesh grid.[48–50] The EDS results for the $MgAl_2O_4$:Ce and $MgAl_2O_4$:Ce:Mn samples show characteristic peaks of the corresponding elements with no other impurity.

The color and optical properties of the $MgAl_2O_4$:Ce and $MgAl_2O_4$:Ce:Mn samples are important to study their photocatalytic activity for degradation of organic dyes. Figure 4a shows the UV–Vis diffuse reflectance spectra of the $MgAl_2O_4$:Ce and $MgAl_2O_4$:Ce:Mn samples. In the ultraviolet region ($\lambda < 400$ nm), low reflectance of the $MgAl_2O_4$:Ce and $MgAl_2O_4$:Ce:Mn samples was observed. In the visible region ($\lambda > 400$ nm), a continuous increase

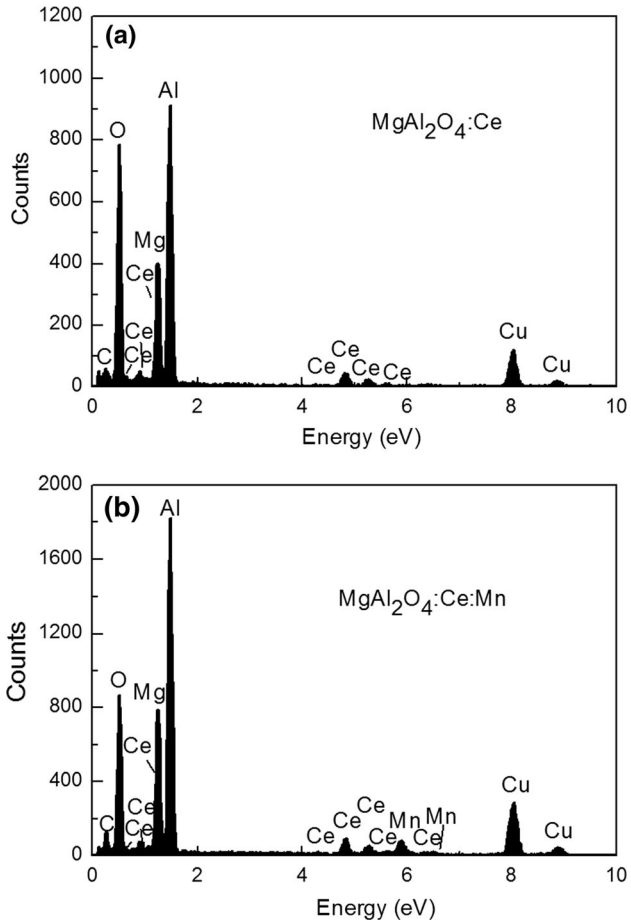

Fig. 3. EDS results of (a) $MgAl_2O_4$:Ce and (b) $MgAl_2O_4$:Ce:Mn samples.

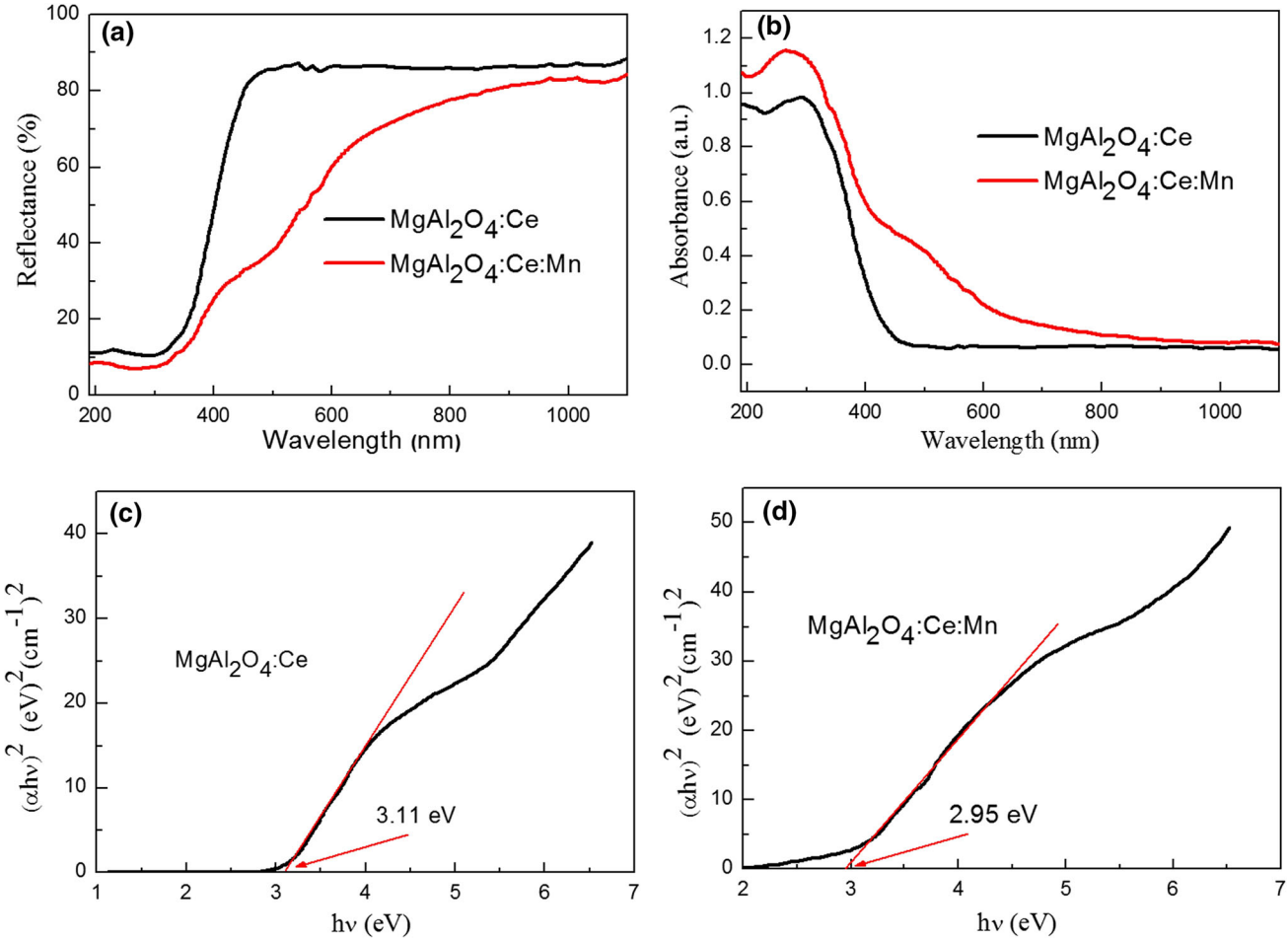

Fig. 4. (a) UV–Vis diffuse reflectance spectra and (b) UV–Vis absorption spectra of $MgAl_2O_4$:Ce and $MgAl_2O_4$:Ce:Mn samples. Optical bandgap (E_g) values of the corresponding (c) $MgAl_2O_4$:Ce and (d) $MgAl_2O_4$:Ce:Mn samples.

Table I. Color coordinates and E_g value of $MgAl_2O_4$:Ce and $MgAl_2O_4$:Ce:Mn samples

	Color Coordinates						
Sample	L^*	a^*	b^*	c^*	$H°$	E_{CIE}^*	**E_g Value (eV)**
$MgAl_2O_4$[9]	98.262	−0.306	2.730	2.747	−83.605	98.300	3.923
$MgAl_2O_4$:Ce	94.238	−2.917	6.237	6.885	−64.935	94.489	3.110
$MgAl_2O_4$:Ce:Mn	75.624	8.436	20.142	21.837	67.275	78.714	2.950

in reflectance for the two samples was found up to 1100 nm, with the difference that the reflectance of the $MgAl_2O_4$:Ce sample increased rapidly up to 420 nm but remained almost unchanged thereafter. The color coordinates (L^*, a^*, b^*), chroma (c^*), hue angle ($H°$), and total color difference (E_{CIE}^*) of the $MgAl_2O_4$, $MgAl_2O_4$:Ce and $MgAl_2O_4$:Ce:Mn samples were obtained from literature[44,51] and are presented in Table I. The L^* and E_{CIE}^* values decreased with increasing doping, while the b^*, c^*, and $H°$ values showed the opposite trend, while a random behavior is observed for the a^* value in Table I.

To study the light harvesting capacity of the $MgAl_2O_4$:Ce and $MgAl_2O_4$:Ce:Mn samples, their UV–Vis absorption spectra were obtained based on the UV–Vis diffuse reflectance spectra and Kubelka–Munk (K–M) theory, as shown in Fig. 4b. For the $MgAl_2O_4$:Ce sample, the absorption peak appearing in the range of 250 nm to 450 nm can be assigned to defects in the host material.[52] For the $MgAl_2O_4$:Ce:Mn sample, two obvious absorption peaks at 280 nm and 500 nm were found. The absorption peaks at 279 nm and 450 nm can be assigned to *d–d* transition of Mn ion.[31,53,54] The absorption peak range of the magnesium aluminate

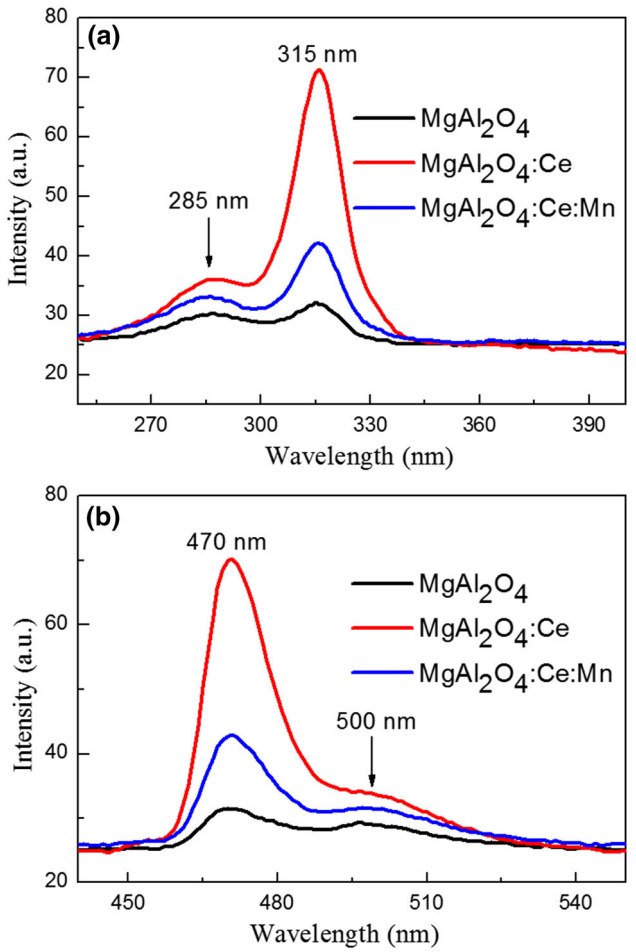

Fig. 5. (a) Excitation and (b) emission spectra of $MgAl_2O_4$, $MgAl_2O_4$:Ce, and $MgAl_2O_4$:Ce:Mn samples.

was extended by codoping with Ce and Mn.[9] These results imply that the $MgAl_2O_4$:Ce:Mn sample will show high visible-light photocatalytic activity.

The bandgap energy (E_g) values of the $MgAl_2O_4$:Ce and $MgAl_2O_4$:Ce:Mn samples were estimated from the absorbance data by using the Tauc relation,

$$(F(R)h\nu)^n = A(h\nu - E_g), \quad (1)$$

where ν, E_g, and A are the frequency, the bandgap energy value, and the absorption coefficient, respectively. n is equal to 2 or l/2 for a direct- and indirect-bandgap semiconductor, respectively. The E_g values of the $MgAl_2O_4$:Ce and $MgAl_2O_4$:Ce:Mn samples were obtained from the intercept of the straight line of the $(F(R)h\nu)^2$ versus $(h\nu)$ plot, as shown in Fig. 4c and d. The E_g values of the $MgAl_2O_4$:Ce and $MgAl_2O_4$:Ce:Mn samples were found to be 3.11 eV and 2.95 eV, respectively. According to Table I, the E_g value decreased with increasing doping. Generally, the E_g value of semiconductor materials decreases with increasing particle size due to the quantum size effect. However, in these experiments, the opposite phenomenon was observed due to the synergistic effects of Ce^{4+}, Mn^{4+}, and $MgAl_2O_4$.

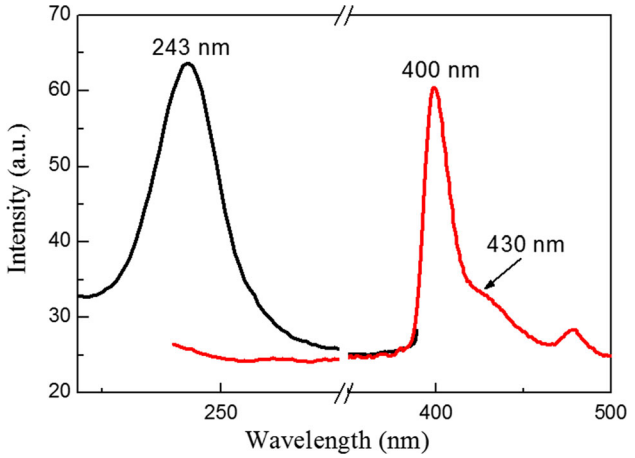

Fig. 6. Excitation and emission spectra of $MgAl_2O_4$:Ce:Mn samples.

Figure 5a shows the excitation spectra of the $MgAl_2O_4$, $MgAl_2O_4$:Ce, and $MgAl_2O_4$:Ce:Mn samples. The excitation spectra were recorded using the emission wavelength of 470 nm. Two excitation peaks at about 285 nm and 315 nm could be observed for the three samples. The excitation peak intensity decreased with increasing doping. Figure 5b shows the emission spectra of the $MgAl_2O_4$, $MgAl_2O_4$:Ce, and $MgAl_2O_4$:Ce:Mn samples. Two obvious emission peaks at 470 nm and 500 nm can be found for the three samples. It can also be seen that the emission peak intensity decreased with increasing doping. Tabaza et al.[13] synthesized Ce-doped $MgAl_2O_4$ by a combustion method, observing a broad green emission band centered at 500 nm under excitation at wavelength of 350 nm. Izumi et al.[55] prepared transition-metal-doped $MgAl_2O_4$ single crystals by the floating zone method, observing different emission peaks with corresponding excitation wavelength. The emission peaks at 490 nm and 505 nm can be ascribed to charge-transfer deexcitation.[55] Sakuma et al.[29] synthesized Mn-doped $MgAl_2O_4$ spinel crystals by the floating zone technique, observing that the peak wavelength (> 512 nm) increased with increasing x (x = MgO/Al_2O_3) because of the variation of the crystal field energy with the composition. Lin et al.[30] prepared hexagonal $MgAl_2O_4$:Mn^{2+} nanoplates using a simple two-step method, observing an emission peak at 568 nm under excitation of 390 nm due to the transition from the excited $^4T_1$ (4G) state to the ground $^6A_1$ (6S) state level of Mn^{2+}. Zhong et al.[31] found that $MgAl_2O_4$:Mn^{2+} fabricated by high-temperature solid-state reaction between phosphor powder and nanoparticles or a combustion method exhibited different emission peaks with different excitation wavelengths. Zhong[31] and Hanamura et al.[56] stated that the emission peak at 519 nm under excitation at wavelength of 278 nm can be ascribed to radiative transition from the first excitation state $^4T_1$ to the ground state of Mn^{2+}. It can be seen that the photoluminescence properties of $MgAl_2O_4$:Mn^{2+} phosphor strongly depend on the

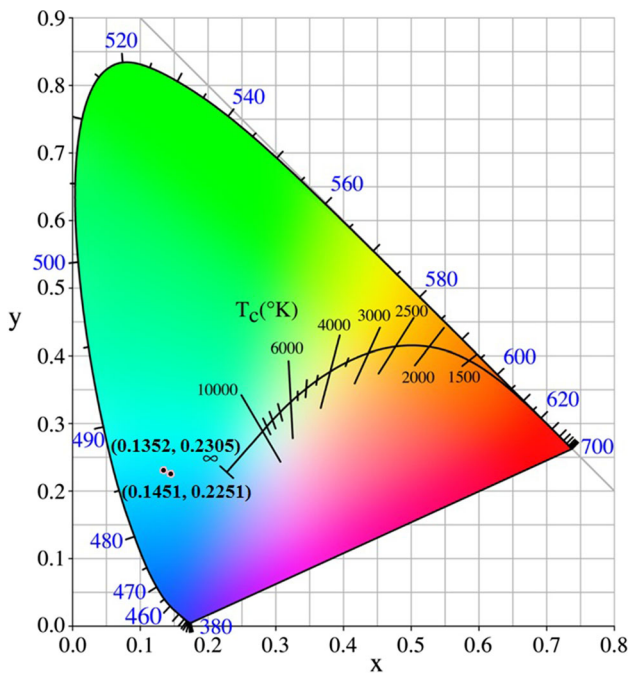

Fig. 7. CIE diagram of $MgAl_2O_4$:Ce and $MgAl_2O_4$:Ce:Mn samples.

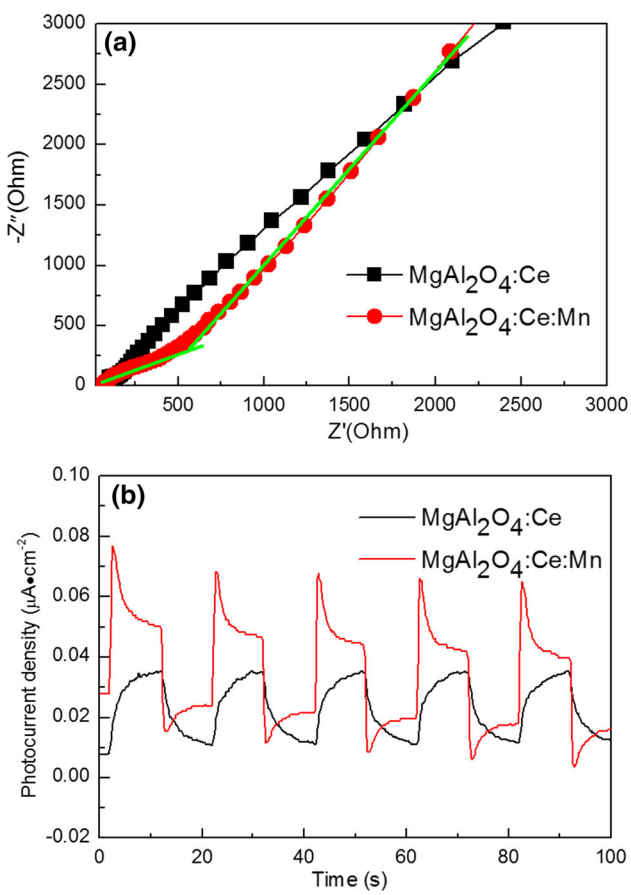

Fig. 8. (a) Electrochemical impedance spectroscopy (EIS) spectra and (b) photocurrent response of $MgAl_2O_4$:Ce and $MgAl_2O_4$:Ce:Mn samples.

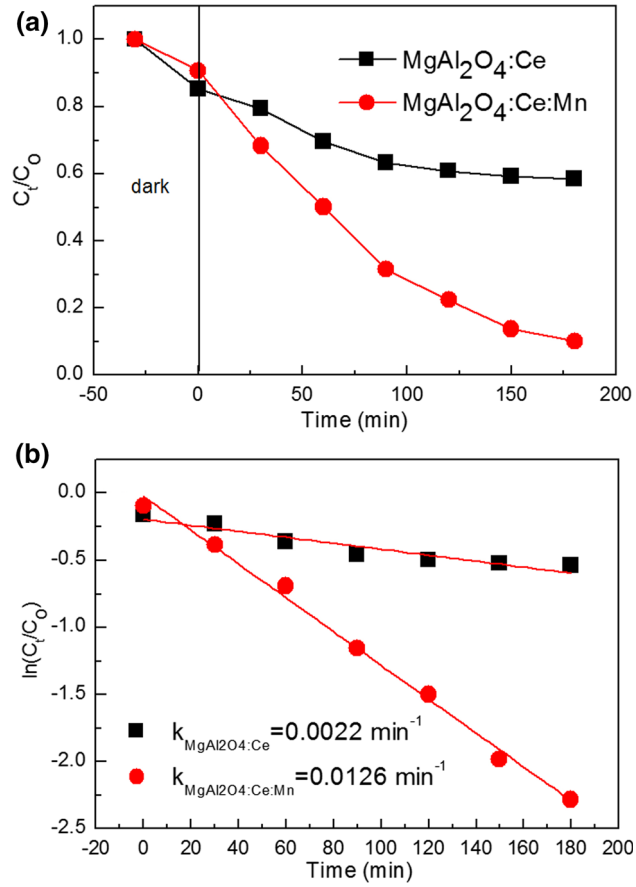

Fig. 9. (a) Time-dependent photocatalytic degradation of MB in presence of $MgAl_2O_4$:Ce and $MgAl_2O_4$:Ce:Mn samples under simulated sunlight irradiation; (b) Plots of $\ln(C/C_0)$ versus irradiation time for $MgAl_2O_4$:Ce and $MgAl_2O_4$:Ce:Mn samples.

synthesis method applied. Sai et al.[57] synthesized Mn/Cr-codoped $MgAl_2O_4$ phosphors, observing strong photoluminescence properties due to energy transfer from Mn^{2+} to Cr^{3+}. In this case, the emission intensity of $MgAl_2O_4$:Ce:Mn was weaker than that of the $MgAl_2O_4$:Ce sample. This result indicates that the Mn^{4+} ion did not have a sensitization effect on Ce^{4+}.

Figure 6 shows the excitation and emission spectra of the $MgAl_2O_4$:Ce:Mn samples, showing an obvious excitation peak at 243 nm and two emission peaks at 400 nm and 430 nm. The excitation peak at 243 nm can be assigned to transitions from $^6A_1(6S)$ to $^4T_1$ level of Mn ion.[53,54] The emission peaks at 400 nm and 430 nm can be ascribed to radiative transition from $^4T_1$ to the ground state of Mn ion.[31] This result further indicates the lack of energy transfer between Ce^{4+} and Mn^{4+}.

Figure 7 shows the CIE diagram of the $MgAl_2O_4$:Ce and $MgAl_2O_4$:Ce:Mn samples. Based on CIE1931 chromaticity software, the color coordinates (x, y) of the $MgAl_2O_4$:Ce and $MgAl_2O_4$:Ce:Mn samples were calculated using the corresponding emission spectra (Fig. 5b). The typical (x, y) color coordinates of the $MgAl_2O_4$:Ce and $MgAl_2O_4$:Ce:Mn

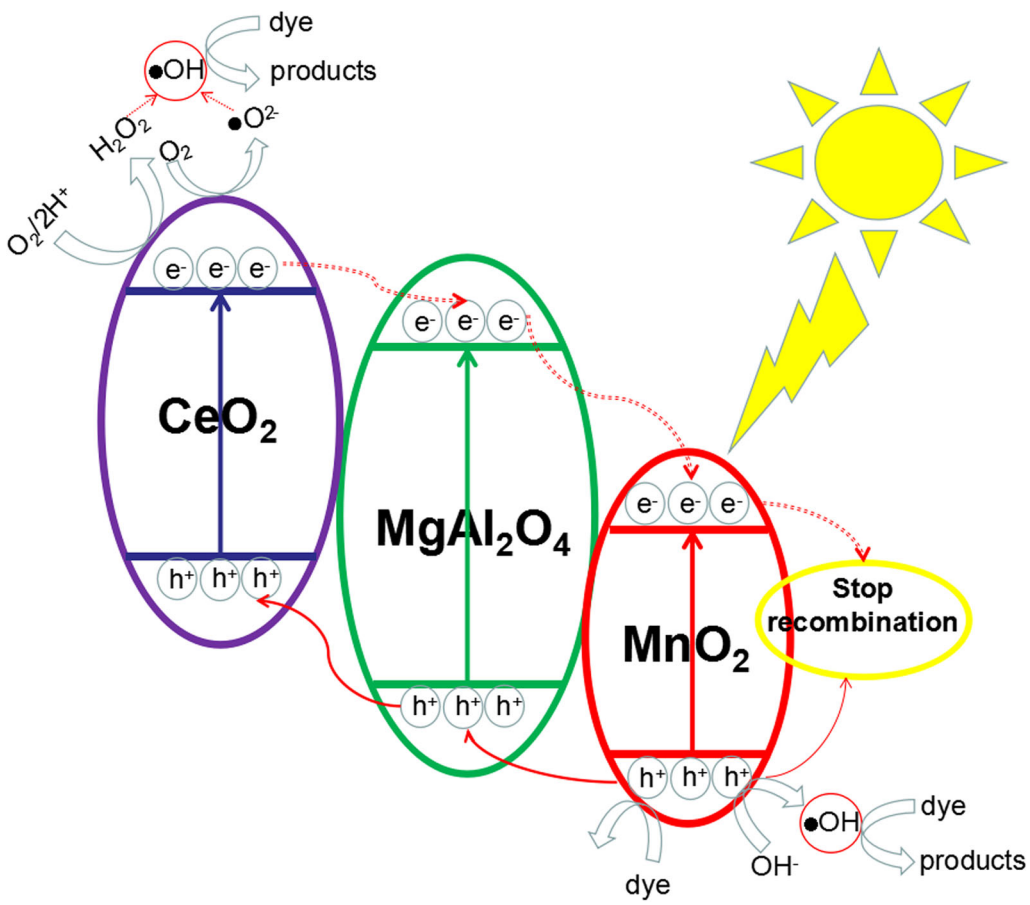

Fig. 10. Electron (e^-)–hole (h^+) separation and energy band matching of ternary $MgAl_2O_4/CeO_2/MnO_2$ heterostructure under simulated sunlight irradiation.

samples were found to be (0.1352, 0.2305) and (0.1451, 0.2251), respectively. Compared with the $MgAl_2O_4$:Ce sample, the color coordinates of the Mn-codoped $MgAl_2O_4$:Ce phosphor moved toward the blue region.

Typical Nyquist plots of the impedance data of the $MgAl_2O_4$:Ce and $MgAl_2O_4$:Ce:Mn samples under simulated sunlight irradiation are shown in Fig. 8a. The $MgAl_2O_4$:Ce sample showed only a straight line, which can be ascribed to the Warburg impedance.[48,58–61] The $MgAl_2O_4$:Ce:Mn sample clearly exhibited a straight line at low frequencies and a semicircle at high frequencies, which can be assigned to the Warburg impedance and charge transfer,[58–61] respectively. The smaller semicircle for the $MgAl_2O_4$:Ce:Mn sample indicates higher photocatalytic activity for degradation of organic dyes. The photocurrent response curve of the semiconductor can also be used to determine the photocatalytic activity of the material. The photocurrent response of the $MgAl_2O_4$:Ce and $MgAl_2O_4$:Ce:Mn samples is shown in Fig. 8b. For the $MgAl_2O_4$:Ce sample, the photocurrent response can be assigned to electron transfer between $MgAl_2O_4$ and Ce oxide. The photocurrent intensity of the $MgAl_2O_4$:Ce:Mn sample is higher than that of the $MgAl_2O_4$:Ce sample. The enhanced photocurrent for the $MgAl_2O_4$:Ce:Mn sample indicates that it is expected to show higher photocatalytic activity due to the electron transfer and higher separation efficiency of electrons and holes.

To compare the photocatalytic activity of the $MgAl_2O_4$, $MgAl_2O_4$:Ce, and $MgAl_2O_4$:Ce:Mn samples, methylene blue was chosen as a target dye for degradation. Figure 9a shows the time-dependent photocatalytic degradation of MB dye in presence of $MgAl_2O_4$:Ce and $MgAl_2O_4$:Ce:Mn samples under simulated sunlight irradiation. The degradation rate of both $MgAl_2O_4$:Ce and $MgAl_2O_4$:Ce:Mn samples increased with increasing irradiation time. The photocatalytic activity of the $MgAl_2O_4$, $MgAl_2O_4$:Ce, and $MgAl_2O_4$:Ce:Mn samples followed the order: $MgAl_2O_4$:Ce:Mn > $MgAl_2O_4$ > $MgAl_2O_4$:Ce. This result confirms that the $MgAl_2O_4$:Ce:Mn sample exhibited the highest photocatalytic activity due to the wide and strong absorption band in the range of 190 nm to 700 nm. Note that the $MgAl_2O_4$:Ce:Mn sample showed lower emission intensity than the $MgAl_2O_4$:Ce sample. The photocatalytic activity of semiconductor materials is mainly governed by crystal structure, type of doped ion, surface morphology, band-edge position, light absorption

capacity and utilization, and separation efficiency of photogenerated carriers.[38,62] Although formation of $MgAl_2O_4$ phase was inhibited, there was no significant change in the spinel structure of $MgAl_2O_4$ after introduction of Ce^{4+} or Ce^{4+} and Mn^{4+}. Therefore, the important reasons for the observed differences are the type of doped ion, surface morphology, band-edge position, light absorption capacity and utilization, and separation efficiency of photogenerated carriers. The smaller particle size of the $MgAl_2O_4$:Ce:Mn nanoparticles would increase their specific surface area and possibly the photocatalytic activity.[32] As confirmed by the TEM, UV–Vis absorption, emission spectra, and electrochemistry analysis results presented above, the $MgAl_2O_4$:Ce:Mn sample had a relatively lower E_g value, particle size, and emission intensity but higher utilization and separation efficiency, indicating that it has excellent visible light absorption capacity with a lower recombination rate of photogenerated carriers.

The first-order kinetics for the photocatalytic degradation of methylene blue dye by the $MgAl_2O_4$:Ce and $MgAl_2O_4$:Ce:Mn samples can be fit by a first-order model as described by Eq. 2.[63]

$$\ln(C_t/C_0) = -kt, \tag{2}$$

where C_t, C_0, k, and t are the apparent concentration of methylene blue dye after degradation, initial concentration of methylene blue dye, kinetic rate constant, and degradation time, respectively. The values of k for the $MgAl_2O_4$:Ce and $MgAl_2O_4$:Ce:Mn samples were evaluated from the slope and intercept of the linear plot, as shown in Fig. 9b. The rate constant (k) for the $MgAl_2O_4$, $MgAl_2O_4$:Ce and $MgAl_2O_4$:Ce:Mn samples was found to be 0.0053 min^{-1},[9] 0.0022 min^{-1}, and 0.0126 min^{-1}, respectively. These results reveal that the $MgAl_2O_4$:Ce:Mn sample exhibited 5.73 times higher activity for photocatalytic degradation of methylene blue dye compared with the $MgAl_2O_4$:Ce sample.

To study the photocatalytic mechanism of the $MgAl_2O_4$:Ce:Mn sample, the conduction-band (CB) and valence-band (VB) potentials of $MgAl_2O_4$, CeO_2, and MnO_2 were calculated using Eqs. 3 and 4.

$$E_{CB} = X - E^e - 0.5E_g, \tag{3}$$

$$E_{VB} = X - E^e + 0.5E_g, \tag{4}$$

where E^e is 4.5 eV and X for CeO_2 and MnO_2 is estimated as 4.986 eV and 5.958 eV by using Eqs. 5 and 6, respectively. The E_g values of $MgAl_2O_4$, CeO_2, and MnO_2 are found to be 3.923 eV,[9] 3.230 eV,[64] and 2.400 eV,[65] respectively.

$$X(CeO_2) = \sqrt[3]{X(Ce)X(O)^2}, \tag{5}$$

$$X(MnO_2) = \sqrt[3]{X(Mn)X(O)^2}, \tag{6}$$

where X(Ce) = 2.18 eV, X(Mn) = 3.72 eV, and X(O) = 7.54 eV. The CB potentials of $MgAl_2O_4$, CeO_2, and MnO_2 are estimated as −1.0965, −1.1290, and 0.2580 V, respectively, with corresponding VB potentials of 2.5025 V, 2.1010 V, and 2.6580 V. Figure 10 shows the electron (e^-)–hole (h^+) separation and energy band matching of the ternary $MgAl_2O_4/CeO_2/MnO_2$ heterostructure under simulated sunlight irradiation. When the $MgAl_2O_4$:Ce:Mn photocatalyst is irradiated with simulated sunlight, an electron (e^-) transition occurs from the VB of MnO_2 to the VB of $MgAl_2O_4$ then to the VB of CeO_2 and finally to the CB, leaving holes in the VB of each oxide and thus creating electron–hole pairs. The relevant reaction can be described as follows:

$$MgAl_2O_4{:}Ce{:}Mn + h\nu \rightarrow MgAl_2O_4{:}Ce{:}Mn(e^- + h^+) \tag{7}$$

In this photocatalytic system, the h^+ and e^- of $MgAl_2O_4$:Ce:Mn can react with OH^- or dye and O_2/H_2O or O_2 to generate $^{\cdot}OH$ radicals as the redox potential of OH^-/OH, O_2/H_2O_2, and O_2/O^{2-} is +1.89 V, +0.695 V, and −0.13 V versus normal hydrogen electrode (NHE),[66–72] respectively. The related photocatalytic reaction process can be described by reactions (8)–(15).

$$h^+_{VB} + OH^- \rightarrow {}^{\cdot}OH \tag{8}$$

$$H^+ + \text{dye} \rightarrow \text{degradation products} \tag{9}$$

$$e^-_{CB} + O_2 \rightarrow {}^{\cdot}O^{2-} \tag{10}$$

$${}^{\cdot}O^{2-} + 2H^+ + e^-_{CB} \rightarrow H_2O_2 \tag{11}$$

$$2e^-_{CB} + O_2 + 2H^+ \rightarrow H_2O_2 \tag{12}$$

$$e^-_{CB} + H_2O_2 \rightarrow {}^{\cdot}OOH + OH^- \tag{13}$$

$${}^{\cdot}O^{2-} + H_2O_2 \rightarrow {}^{\cdot}OOH + OH^- + O_2 \tag{14}$$

$${}^{\cdot}OH + \text{dye} \rightarrow \text{degradation products} \tag{15}$$

It can be seen that the band-edge position of the photocatalytic system was extended by codoping of cerium and manganese ions into magnesium aluminate. Therefore, recombination of electron–hole pairs is prevented, enhancing the photon utilization rate of the $MgAl_2O_4$:Ce:Mn and improving its photocatalytic activity.

CONCLUSIONS

$MgAl_2O_4$:Ce:Mn photocatalyst was successfully synthesized by using a modified polyacrylamide gel method. XRD analysis indicated that the spinel structure of $MgAl_2O_4$ was not changed by the introducing of Ce^{4+} or Ce^{4+} and Mn^{4+}. The $MgAl_2O_4$:Ce:Mn sample showed a relatively lower E_g value, particle size, and emission intensity but higher utilization and separation efficiency compared with the $MgAl_2O_4$:Ce sample. In addition, the $MgAl_2O_4$:Ce:Mn sample exhibited excellent visible-light absorption capacity and lower recombination rate of photogenerated carriers. $MgAl_2O_4$:Ce:Mn nanoparticles could be used as a photocatalyst for photodegradation of methylene blue dye under simulated sunlight irradiation. The high photocatalytic activity of the $MgAl_2O_4$:Ce:Mn nanoparticles can be ascribed to the synergistic effects of the band-edge position, light absorption capacity and utilization, and separation efficiency of photogenerated carriers.

ACKNOWLEDGMENTS

This work was supported by the Talent Introduction Project (09924601), Major Cultivation Projects (18ZDPY01), and Research project of higher education teaching reform (JGZC1903) of Chongqing Three Gorges University, the Chongqing basic research and frontier exploration (general project) (cstc2019jcyj-msxm1327).

CONFLICT OF INTEREST

The authors declare that they have no competing interests.

REFERENCES

1. A. Pille, H. Spiridigliozzi, M. Amamra, T. Billeton, M. Zaghrioui, E. Feldbach, A. Kanaeva, and F. Schoenstein, *Ceram. Int.* 45, 8305 (2019).
2. M.J. Iqbal, B. Ismail, C. Rentenberger, and H. Ipser, *Mater. Res. Bull.* 46, 2271 (2011).
3. M. Han, Z. Wang, Y. Xu, R. Wu, S. Jiao, Y. Chen, and S. Feng, *Mater. Chem. Phys.* 215, 251 (2018).
4. N. Obradović, W.G. Fahrenholtz, S. Filipović, D. Kosanović, A. Dapčević, A. Đorđević, I. Balać, and V.B. Pavlović, *Ceram. Int.* 45, 12015 (2019).
5. S.K. Hg, S.G. Menon, D. Hebbar, K.S. Choudhari, C. Santhosh, and S.D. Kulkarni, *Mater. Res. Bull.* 111, 294 (2019).
6. T. Shiono, K. Shiono, K. Miyamoto, and G. Pezzotti, *J. Am. Ceram. Soc.* 83, 235 (2000).
7. S. Benaissa, M. Hamidouche, M. Kolli, G. Bonnefont, and G. Fantozzi, *Ceram. Int.* 42, 8839 (2016).
8. A. Goldstein, P. Loiko, Z. Burshtein, N. Skoptsov, I. Glazunov, E. Galun, N. Kuleshov, and K. Yumashev, *J. Am. Ceram. Soc.* 1331, 1324 (2016).
9. S. Wang, H. Gao, Y. Wei, Y. Li, X. Yang, L. Fang, and L. Lei, *CrystEngComm* 21, 263 (2019).
10. A. Kobylinska, K. Kniec, and L. Marciniak, *New J. Chem.* 43, 6080 (2019).
11. Z. Wang, Y. Xu, Q. Zhang, Y. Chen, G. Pang, and S. Feng, *J. Lumin.* 211, 108 (2019).
12. D. Valiev, S. Stepanov, O. Khasanov, E. Dvilis, E. Polisadova, and V. Paygin, *Opt. Mater.* 91, 396 (2019).
13. W.A.I. Tabaza, H.C. Swart, and R.E. Kroon, *Phys. B* 439, 109 (2014).
14. S.C. Xu, P.L. Li, Z.J. Wang, T. Li, Q.Y. Bai, J. Sun, and Z.P. Yang, *J. Mater. Chem. C* 3, 9112 (2015).
15. Q. Bao, Z.J. Wang, J. Sun, Z.P. Wang, X.Y. Meng, K.L. Qiu, Y. Chen, Z.P. Yang, and P.L. Li, *Dalton Trans.* 47, 13913 (2018).
16. S.C. Xu, Z.J. Wang, P.L. Li, T. Li, Q.Y. Bai, J. Sun, and Z.P. Yang, *J. Am. Ceram. Soc.* 100, 2069 (2017).
17. T. Li, P.L. Li, Z.J. Wang, S.C. Xu, Q.Y. Bai, and Z.P. Yang, *J. Phys. Chem. C* 120, 20254 (2016).
18. S.C. Xu, Z.J. Wang, P.L. Li, T. Li, Q.Y. Bai, and Z.P. Yang, *Spectrochim. Acta A* 199, 228 (2018).
19. K.L. Qiu, Z.J. Wang, J.M. Shi, Y.L. Sun, N. Jiang, M.M. Tian, X.Y. Meng, Z.P. Yang, and P.L. Li, *Spectrochim. Acta A* 213, 141 (2019).
20. T. Li, P.L. Li, Z.J. Wang, S.C. Xu, Q.Y. Bai, and Z.P. Yang, *Phys. Chem. Chem. Phys.* 19, 4131 (2017).
21. X. Li, Z.J. Wang, J.J. Liu, X.Y. Meng, K.L. Qiu, Q. Bao, Y.B. Li, Z.P. Wang, Z.P. Yang, and P.L. Li, *Inorg. Chem.* 57, 13783 (2018).
22. C. Wang, Z. Wang, J. Cheng, Z. Li, M. Tian, Z. Yang, and P. Li, *CrystEngComm* 20, 7156 (2018).
23. C. Wang, Z. Wang, P. Li, J. Cheng, Z. Li, M. Tian, Y. Sun, and Z. Yang, *J. Mater. Chem. C* 5, 10839 (2017).
24. X. Li, P.L. Li, Z.J. Wang, S.M. Liu, Q. Bao, X.Y. Meng, K.L. Qiu, Y.B. Li, Z.Q. Li, and Z.P. Yang, *Chem. Mater.* 29, 8792 (2017).
25. P.L. Li, Z.J. Wang, Z.P. Yang, and Q.L. Guo, *J. Mater. Chem. C* 2, 7823 (2014).
26. Y.S. Sun, P.L. Li, Z.J. Wang, J. Cheng, Z.L. Li, C. Wang, M.M. Tian, and Z.P. Yang, *J. Phys. Chem. C* 120, 20254 (2016).
27. R.Z. Gu, M.Y. Guan, N. Jiang, T.Y. Yuan, G.Q. Ma, C. Wang, Z.P. Yang, P.L. Li, and Z.J. Wang, *J. Alloys Compd.* 775, 393 (2019).
28. C. Wang, P.L. Li, Z.J. Wang, Y.S. Sun, J.G. Cheng, Z.L. Li, M.M. Tian, and Z.P. Yang, *Phys. Chem. Chem. Phys.* 18, 28661 (2016).
29. T. Sakuma, S. Minowa, T. Katsumata, S. Komuro, and H. Aizawa, *Opt. Mater.* 37, 302 (2014).
30. J. Lin, Y. Huang, J. Zhang, F. Shi, S. Wei, J. Gao, and X. Ding, *Mater. Res. Bull.* 44, 106 (2009).
31. R. Zhong, J. Zhang, H. Wei, X. Qi, M. Li, and X. Han, *Chem. Phys. Lett.* 508, 207 (2011).
32. R.J. Dillon, J.B. Joo, F. Zaera, Y. Yin, and C.J. Bardeen, *Phys. Chem. Chem. Phys.* 15, 1488 (2013).
33. Z. Wei, R. Li, and R. Wang, *RSC Adv.* 8, 7956 (2018).
34. L. Zhang and H. Yang, *Appl. Phys. A* 98, 801 (2010).
35. Q. Xiao, Z. Si, J. Zhang, C. Xiao, Z. Yu, and G. Qiu, *J. Mater. Sci.* 42, 9194 (2007).
36. L.Q. Jing, X.J. Sun, B.F. Xu, B.Q. Wang, W.M. Cai, and H.G. Fu, *J. Solid State Chem.* 177, 3375 (2004).
37. R. Sellappan, A. Galeckas, V. Venkatachalapathy, A.Y. Kuznetsov, and D. Chakarov, *Appl. Catal. B Environ.* 106, 337 (2011).
38. L. Cai, Q. Long, and C. Yin, *Appl. Surf. Sci.* 319, 60 (2014).
39. S.F. Wang, H. Lv, X.S. Zhou, Y.Q. Fu, and X.T. Zu, *Nanosci. Nanotechnol. Lett.* 6, 758 (2014).
40. H. Yang, Z.E. Cao, X. Shen, T. Xian, W.J. Feng, J.L. Jiang, Y.C. Feng, Z.Q. Wei, and J.F. Dai, *J. Appl. Phys.* 106, 104317 (2009).
41. H. Zhang, X. Fu, S. Niu, G. Sun, and Q. Xin, *J. Solid State Chem.* 177, 2649 (2004).
42. X. Fu, H. Zhang, S. Niu, and Q. Xin, *J. Solid State Chem.* 178, 603 (2005).
43. S. Wang, D. Li, C. Yang, G. Sun, J. Zhang, and Y. Xia, *J. Sol–Gel. Sci. Technol.* 84, 169 (2017).
44. H.J. Gao, H. Yang, S.F. Wang, D. Li, F. Wang, and L.M. Fang, *J. Sol–Gel. Sci. Technol.* 86, 206 (2018).
45. R.J. Wiglusz, T. Grzyb, S. Lis, and W. Strek, *J. Nanosci. Nanotechnol.* 9, 5803 (2009).
46. W.H. Bragg, *Philos. Mag.* 30, 305 (1915).
47. S. Nishika, *Proc. Math. Phys. Soc. Tokyo* 8, 199 (1915).

48. Z. Cui, H. Yang, and X. Zhao, *Mater. Sci. Eng. B Adv.* 229, 160 (2018).
49. Y. Xia, Z. He, K. Hu, B. Tang, and X. Li, *J. Alloys Compd.* 753, 356 (2018).
50. L.J. Di, H. Yang, T. Xian, and X.J. Chen, *Nanoscale Res. Lett.* 13, 257 (2018).
51. H. Gao, H. Yang, S. Wang, and X. Zhao, *Ceram. Int.* 44, 14754 (2018).
52. S.V. Motloung, B.F. Dejene, O.M. Ntwaeaborwa, H.C. Swart, and R.E. Kroon, *Chem. Phys.* 487, 75 (2017).
53. A. Tomita, T. Sato, K. Tanaka, Y. Kawabe, M. Shirai, K. Tanaka, and E. Hanamura, *J. Lumin.* 109, 19 (2004).
54. S. Vijay, R.P.S. Chakradhar, and J.L. Rao, *J. Solid State Chem.* 180, 2067 (2007).
55. K. Izumi, S. Miyazaki, S. Yoshida, T. Mizokawa, and E. Hanamura, *Phys. Rev. B* 76, 075111 (2007).
56. E. Hanamura, Y. Kawabe, H. Takashima, T. Sato, and A. Tomita, *J. Nonlinear Opt. Phys.* 12, 467 (2003).
57. Q. Sai, C. Xia, H. Rao, X. Xu, G. Zhou, and P. Xu, *J. Lumin.* 131, 2359 (2011).
58. X.X. Zhao, H. Yang, H.M. Zhang, Z.M. Cui, and W.J. Feng, *Desalin. Water Treat.* 145, 326 (2019).
59. Y. Xia, Z. He, W. Yang, B. Tang, Y. Lu, and K. Hu, *Mater. Res. Express* 5, 025504 (2018).
60. H. Gao, H. Yang, and S. Wang, *Trans. Indian Ceram. Soc.* 77, 150 (2018).
61. Y. Yan, H. Yang, Z. Yi, R. Li, and X. Wang, *Micromachines* 10, 254 (2019).
62. R.G. Zhu, Y.J. Zhu, M. Zhang, Y. Xiao, X.L. Du, H. Liu, and S.L. Wang, *Mater. Sci. Eng. C* 39, 305 (2014).
63. Y. Xia, Z. He, J. Su, Y. Liu, and B. Tang, *Nanoscale Res. Lett.* 13, 148 (2018).
64. H. Gao, H. Yang, G. Yang, and S. Wang, *Mater. Technol.* 33, 321 (2018).
65. G.A.M. Ali, M.M. Yusoff, E.R. Shaaban, and K.F. Chong, *Ceram. Int.* 43, 8440 (2017).
66. T. Tachikawa, M. Fujitsuka, and T. Majima, *J. Phys. Chem. C* 111, 5259 (2007).
67. S.F. Wang, H.J. Gao, L.M. Fang, Y. Wei, Y.W. Li, and L. Lei, *Z. Phys. Chem.* (2019). https://doi.org/10.1515/zpch-2018-1308.
68. Y. Xia, Z. He, J. Su, B. Tang, and Y. Liu, *J. Mater. Sci. Mater. Electron.* 29, 15271 (2018).
69. H.J. Gao, F. Wang, S.F. Wang, X.X. Wang, Z. Yi, and H. Yang, *Mater. Res. Bull.* 115, 140 (2019).
70. S.Y. Wang, H. Yang, X.X. Wang, and W.J. Feng, *J. Electron. Mater.* 48, 2067 (2019).
71. S.F. Wang, H.J. Gao, C.L. Chen, Y. Wei, and X.X. Zhao, *J. Sol–Gel Sci. Technol.* (2019). https://doi.org/10.1007/s10971-019-05062-8.
72. T. Arai, M. Yanagida, Y. Konishi, Y. Iwasaki, H. Sugihara, and K. Sayama, *J. Phys. Chem. C* 111, 7574 (2007).